

Article

# Bioenergy Generation and Wastewater Purification with $\text{Li}_{0.95}\text{Ta}_{0.76}\text{Nb}_{0.19}\text{Mg}_{0.15}\text{O}_3$ as New Air-Photocathode for MFCs

Noureddine Touach <sup>1,\*</sup>, Abdellah Benzaouak <sup>1</sup>, Jamil Toyir <sup>2</sup>, Adnane El Hamidi <sup>3</sup>, Mohammed El Mahi <sup>1</sup>, El Mostapha Lotfi <sup>1</sup>, Mohamed Kacimi <sup>3</sup> and Leonarda Francesca Liotta <sup>4,\*</sup>

- <sup>1</sup> Laboratory of Spectroscopy, Molecular Modelling, Materials, Nanomaterials, Water and Environment, Environmental Materials Team, École Nationale Supérieure d'Arts et Métiers (ENSAM), Mohammed V University in Rabat, B.P. 6207 Avenue des Forces Armées Royales, Rabat B.P. 1014, Morocco
- <sup>2</sup> Laboratoire des Procédés, Matériaux et Environnement (LPME), Faculté Polydisciplinaire (FP-Taza), Université Sidi Mohammed Ben Abdellah, Taza B.P. 1223, Morocco
- <sup>3</sup> Laboratory of Physical Chemistry of Materials, Catalysis and Environment, Department of Chemistry, Faculty of Sciences, Mohammed V University in Rabat, Rabat B.P. 1014, Morocco
- <sup>4</sup> Istituto per lo Studio dei Materiali Nanostrutturati (ISMN)-CNR, Via Ugo La Malfa, 153, 90146 Palermo, Italy
- \* Correspondence: n.touach@um5r.ac.ma (N.T.); leonardafrancesca.liotta@cnr.it (L.F.L.)

**Abstract:** MFC is a promising technology that can be used for simultaneous electricity generation and wastewater treatment. Power energy generation of a ferroelectric cathodic ceramic,  $\text{Li}_{0.95}\text{Ta}_{0.76}\text{Nb}_{0.19}\text{Mg}_{0.15}\text{O}_3$  (LTNMg), has been measured in microbial fuel cells, integrating a single chamber fed by industrial wastewater ( $\text{COD}_{\text{initial}} = 471 \text{ mg L}^{-1}$ , and  $\text{pH}_{\text{initial}} = 7.24$  at  $T = 27^\circ\text{C}$ ). In this process, the mixed multicomponent oxide material has been prepared and characterized by XRD, PSD, TEM, and UV-Vis spectroscopy. The catalytic activity has been investigated by COD determination, analysis of heavy metals, and polarization measurement. The results show a high COD reduction efficiency, which reaches 95.70% after a working time of 168 h with a maximal power density of  $228 \text{ mW m}^{-2}$ . In addition, the maximum value of generated voltage in the open-circuit potential (OCP) of this MFC configuration has been increased from 340 mV in the absence of a light source to 470 mV under irradiation, indicating the presence of a promoting photocatalytic effect of LTNMg, which improved the process of the cathodic electron transfer inside the MFC device.

**Keywords:** ferroelectric ceramic; MFCs; wastewater treatment; photocatalysis; COD; heavy metals



**Citation:** Touach, N.; Benzaouak, A.; Toyir, J.; El Hamidi, A.; El Mahi, M.; Lotfi, E.M.; Kacimi, M.; Liotta, L.F. Bioenergy Generation and Wastewater Purification with  $\text{Li}_{0.95}\text{Ta}_{0.76}\text{Nb}_{0.19}\text{Mg}_{0.15}\text{O}_3$  as New Air-Photocathode for MFCs. *Catalysts* **2022**, *12*, 1424. <https://doi.org/10.3390/catal12111424>

Academic Editor: Detlef W. Bahnemann

Received: 25 October 2022  
Accepted: 10 November 2022  
Published: 13 November 2022

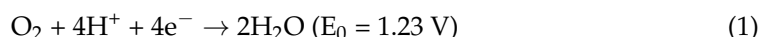
**Publisher's Note:** MDPI stays neutral with regard to jurisdictional claims in published maps and institutional affiliations.



**Copyright:** © 2022 by the authors. Licensee MDPI, Basel, Switzerland. This article is an open access article distributed under the terms and conditions of the Creative Commons Attribution (CC BY) license (<https://creativecommons.org/licenses/by/4.0/>).

## 1. Introduction

Water and energy resource management is currently considered as an interconnected process, implying combined approaches and operational tools that can enhance sustainable development. In this context, the microbial fuel cells (MFCs) technology attracts growing interest due to its potential to integrate a challenging bifunctional process of wastewater treatment coupled with an in situ renewable electric power generation [1,2]. A typical MFC consists of two compartments, an anode and a cathode, separated by a PEM membrane and connected by an external circuit, ensuring the transport of electrons from the anode to the cathode, where they interact with protons and oxygen to form water according to the following reaction [3]:



A continuous consumption of oxygen is then produced to maintain the necessary potential for electricity generation. Oxygen can be provided in the cathode compartment either by bubbling the water or by using an air cathode. The cathodic reaction can be improved by the use of catalytic-coated electrodes. Catalysts are often expensive and rare metals.

Despite the progress made during the last decade in this technology, the performance required to reach a competitive level beyond the pilot scale has yet to be proven. The power output of the MFC depends on several factors, particularly the improvement of the electrode materials [4,5]. Indeed, among the challenges of MFC is the development of low-cost and more efficient catalysts as cathodic components to replace the noble metals recognized as the best catalysts for this bio-electrochemical system to achieve a large-scale production with low cost [6].

From this point of view, many studies have explored several new photocathode materials in MFC devices. However, this process remains a challenge, due to its insufficient low performance [7,8]. Titanium oxide is widely used as a photocathodic catalyst because of its stability, and it is non-toxic and economically less expensive [7,9–11]. However, this material has a major disadvantage blocking its high activity, originating from the side-reactions of intermediate species and the short lifetime of photogenerated electron–hole pairs induced inside the photocatalyst [12,13].

Recently, it has been reported that the materials, having an internal electric field, are good candidates to improve the photocatalytic efficiency [14–16]. In particular, ferroelectric materials, due to their spontaneous polarization in the crystalline phase, form a class of such materials that could improve the separation of photo-induced charge carriers throughout the cell, due to their spontaneous polarization in the crystal. This polarization results from deformed unit cells and from the displacement of the barycenter of the positive and negative charges of the crystal [17,18]. Li(Nb, Ta)O<sub>3</sub> are typical materials in this category recognized by their ferroelectric properties [19].

Ferroelectricity in LiNb(Ta)O<sub>3</sub> materials is directly related to their structure since it is due to a spontaneous asymmetry of charges within the crystal lattice [20]. This property can be controlled by a suitable incorporation with different appropriate metal ions in the mixed oxide matrix. The relationship between ferroelectric behavior and photocatalytic properties has been investigated in several studies involving the incorporation of different metallic elements with various valences (Ag<sup>+</sup>, Cu<sup>2+</sup>, Mg<sup>2+</sup>, W<sup>6+</sup>) into cathodic components for controlling the polarization effect on their optical behavior [21–24]. Moreover, the ions' insertion or substitution approach is one of the promising choices to design new photocatalysts and improve their activities [25].

It has been shown that the addition of Mg to LiTaO<sub>3</sub> and LiNbO<sub>3</sub> considerably changes the optical and luminescent properties [26,27]. Photocatalytic activity is mainly related to optical properties in various processes. Therefore, the present work was undertaken to investigate the photoelectro-catalytic performances of Mg-modified LiNb<sub>1-x</sub>Ta<sub>x</sub>O<sub>3</sub> (x = 0.8) under sunlight within a single-chamber microbial fuel cell, using wastewater feedstock. The purification of the effluent was monitored by the COD reduction and the lowering of the heavy metal content.

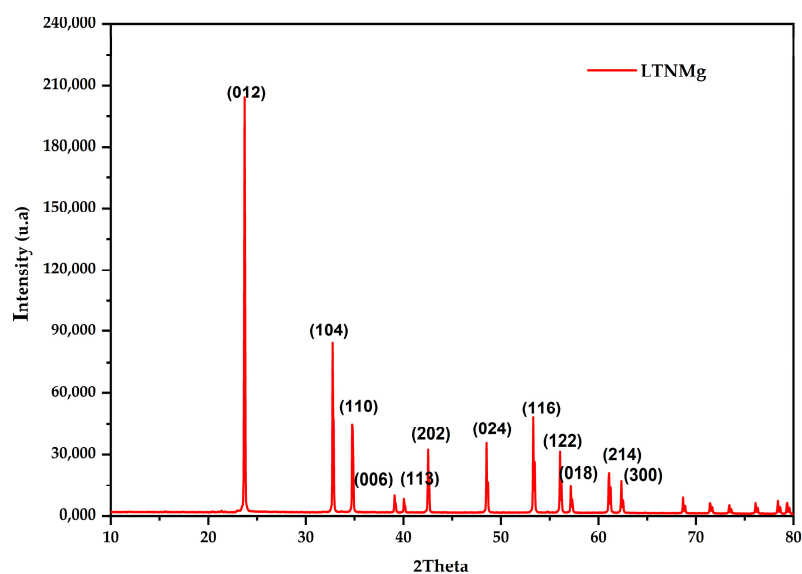
## 2. Results

### 2.1. Cathodic Photocatalyst Characterization

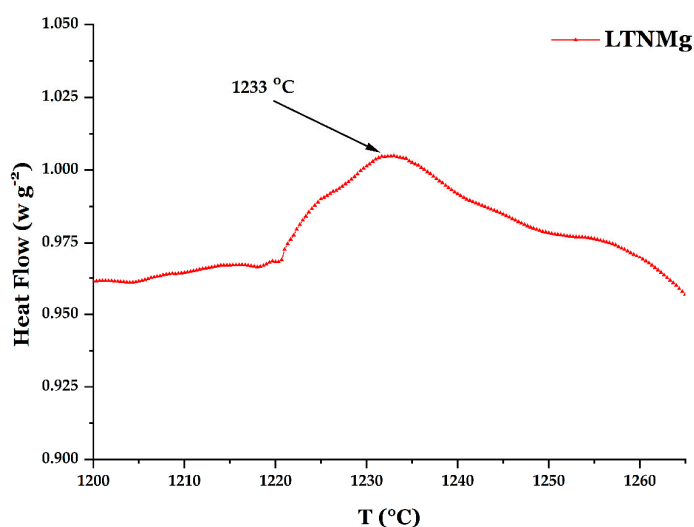
Figure 1 displays the XRD pattern, recorded at ambient conditions, for the LTNMg cathodic material with composition Li<sub>0.95</sub>Ta<sub>0.76</sub>Nb<sub>0.19</sub>Mg<sub>0.15</sub>O<sub>3</sub>. The well-defined diffraction peaks, indicative of a well-crystalline structure, are typical of an isotypic structure, LiTaO<sub>3</sub> (LiNbO<sub>3</sub>), matching the PDF file #04-009-8481, and no impurity peaks were observed. The structure refinement leads to rhombohedral crystallin phase with space group R3c [22,28].

The ferro-para-electric phase transition has been detected by differential scanning calorimetry (DSC) analysis in N<sub>2</sub> atmosphere by increasing the temperature from 800 to 1400 °C (heating rate of 20 °C min<sup>-1</sup>). The recorded DSC profile of the Li<sub>0.95</sub>Ta<sub>0.76</sub>Nb<sub>0.19</sub>Mg<sub>0.15</sub>O<sub>3</sub> sample shows an endothermic peak of high intensity located around 1233 °C (Figure 2). This peak was assigned to the ferroelectric transition of LNTMg. The transition temperature (T<sub>c</sub> = 1233 °C) found in this experiment is very close to that of LiNbO<sub>3</sub> (1165 °C), indicating that the incorporation of Ta<sup>5+</sup> into LiNbO<sub>3</sub> did not disturb the structural property of the

material and its thermodynamics. The values found in this work are comparable to the those reported in previous related studies [29,30].



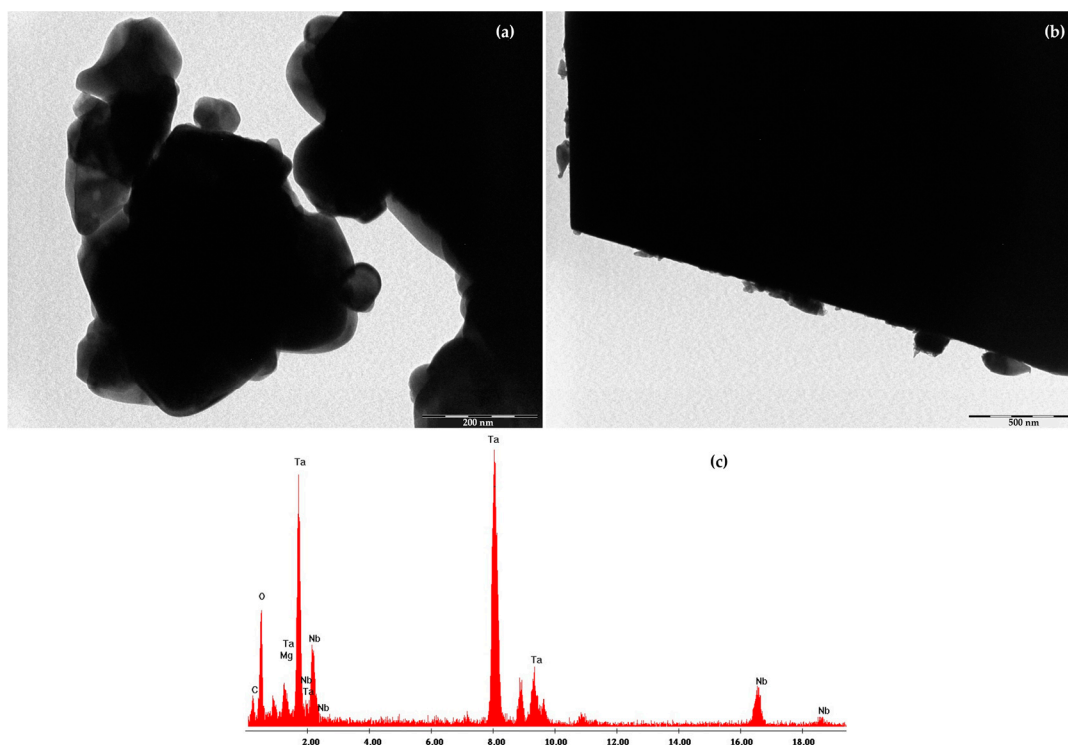
**Figure 1.** XRD pattern of  $\text{Li}_{0.95}\text{Ta}_{0.76}\text{Nb}_{0.19}\text{Mg}_{0.15}\text{O}_3$ .



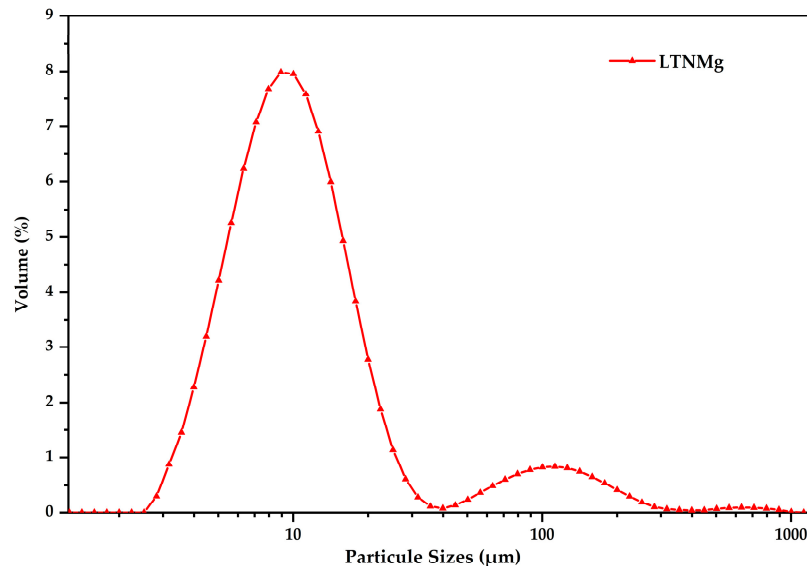
**Figure 2.** Differential scanning calorimetry (DSC) profile of  $\text{Li}_{0.95}\text{Ta}_{0.76}\text{Nb}_{0.19}\text{Mg}_{0.15}\text{O}_3$ .

Figure 3 illustrates the characterization by transmission electron microscopy (TEM) of the  $\text{Li}_{0.95}\text{Ta}_{0.76}\text{Nb}_{0.19}\text{Mg}_{0.15}\text{O}_3$  catalyst before its use in the MFC reaction. The TEM images of the sample show large agglomerated grains (Figure 3a,b), along with small particles on their surfaces. These two different populations of LTNMg clusters are also observed when comparing the TEM analysis to the particle size distribution (PSD) results shown in Figure 4. The particle size varies from 2 to 10  $\mu\text{m}$  for the first population and from 40 to 100  $\mu\text{m}$  for the second population.

Energy-dispersive X-ray (EDX) analysis was applied to identify the composition of the samples. The spectrum shown in Figure 3c indicates the presence of all expected elements (Ta, Nb, O, Mg) except Li, due to its light weight. The presence of carbon in the EDX spectrum originated from the material employed as support for the TEM analysis.



**Figure 3.** (a,b) Transmission electron microscopy and (c) Energy-dispersive X-ray analysis of  $\text{Li}_{0.95}\text{Ta}_{0.76}\text{Nb}_{0.19}\text{Mg}_{0.15}\text{O}_3$  phase.



**Figure 4.** Particle size distribution of the synthesized  $\text{Li}_{0.95}\text{Ta}_{0.76}\text{Nb}_{0.19}\text{Mg}_{0.15}\text{O}_3$  phase.

## 2.2. Optical Properties

The optical properties of the tested photocatalyst were investigated by UV-visible spectrophotometry. Figure 5a depicts the UV-visible absorption spectrum of the LNTMg phase and the Tauc plot. The LNTMg material presents an absorption maximum in the UV region (270 nm), due to  $\text{O}^{2-} \rightarrow \text{M}^{n+}$  electronic transitions ( $\text{M} = \text{Nb}^{5+}, \text{Ta}^{5+}, \text{Mg}^{2+}$ ). The direct bandgap energy ( $E_g$ ) of the sample has been estimated using the linear part of the Tauc plot (Figure 5b). The value of bandgap found for LNTMg ( $E_g \approx 4$  eV) is close to that of  $\text{LiNbO}_3$  (4.08 eV) [22]. It should be noted that in similar works on  $\text{LiTaO}_3$  and LNTCu [28,30], these values were found around 4.81 and 3.5 eV, respectively, revealing that

the addition of Cu to the  $\text{LiNbO}_3\text{-LiTaO}_3$  solid solution shifts the absorption maximum to the visible range. The shift observed with Cu insertion in the solid solution was more important than that produced after Mg incorporation.

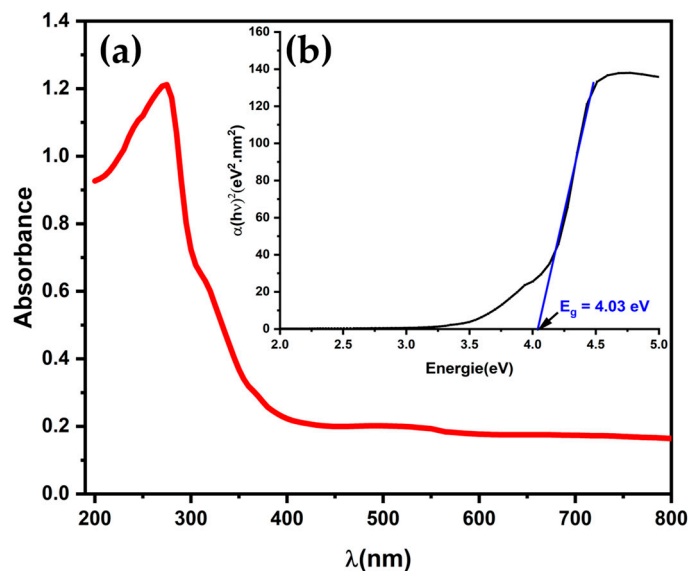


**Figure 5.** (a) UV-Vis absorption spectra of  $\text{Li}_{0.95}\text{Ta}_{0.76}\text{Nb}_{0.19}\text{Mg}_{0.15}\text{O}_3$ . (b) Tauc plot of  $\text{Li}_{0.95}\text{Ta}_{0.76}\text{Nb}_{0.19}\text{Mg}_{0.15}\text{O}_3$ .

### 2.3. Power Performance in Air-Cathode MFCs

The electrodes based on LTNMg were tested in the air cathode MFC systems described below in Figure 6. Polarization data were obtained during the steady phase of operation with a variety of external resistance loads between  $10\ \Omega$  and  $11\ \text{M}\Omega$ . Figure 6 shows the power density and polarization curves of the MFCs after 168 h in operation, with the presence and absence of a UV-Vis light source. The polarization curves in Figure 6a exhibit the coexistence of three types of regions generally observed in MFC systems. The first region ( $0\text{--}250\ \text{mA m}^{-2}$ ) represents a rapid loss zone for potential in the system due to the activation step (phase I), and the rapidly lowered potential is associated with the need for energy to initiate a redox reaction in the considered biological process [31,32]. The second region ( $250\text{--}1800\ \text{mA m}^{-2}$ ), which is the constant potential drop, is associated with the ohmic resistance (phase II). Finally, the third region (from  $1900\ \text{mA m}^{-2}$ ), which is related to concentration losses, is characterized by the dominance of the mass transfer limitations (phase III). The slope of the second region can be related to the internal resistance of the system. A steeper slope of the profile of this phase is related to a higher internal resistance in MFC devices [33,34]. Regarding the power density curves in Figure 6b, the LTNMg MFC-based cathode could perform a maximum power output of  $109\ \text{mW m}^{-2}$  under irradiation and  $228\ \text{mW m}^{-2}$  in the absence of a light source. The photocatalytic effect induced within the LTNMg cathodic system is clearly demonstrated considering the two-fold increase in the photocatalytic activity of LTNMg after its lightning. The power output performance of the MFC is due to an improved oxygen reduction reaction (ORR) inside the cathodic compartment, which is a key step in the global process. Besides, in the presence of a permanent polarization under light irradiation, LTNMg, which is a ferroelectric material, can produce a built-in electric field, which contributes to the separation of charge- or photo-induced carriers. Therefore, this polarization improves the transport of photo-induced electrons at the interface of the catalytic components. According to recent works, this finding can be explained by a positive effect of the catalyst on the photoreduction reaction at the cathode, and therefore on the overall power performance [15,24,35,36]. Interestingly, the internal resistance has been determined using the slope of the phase II polarization curves for each operating condition. The resistance values, for unirradiated and irradiated

catalytic cathode materials, are slightly different (Table 1), indicating that the light source did not significantly impact the resistance. Maximum power density evolution as a function of time is shown in Figure 7. The maximum power density, which corresponds to the stabilization of the voltage response in MFCs after being fed with wastewater, is achieved within the time interval of 100–125 h.

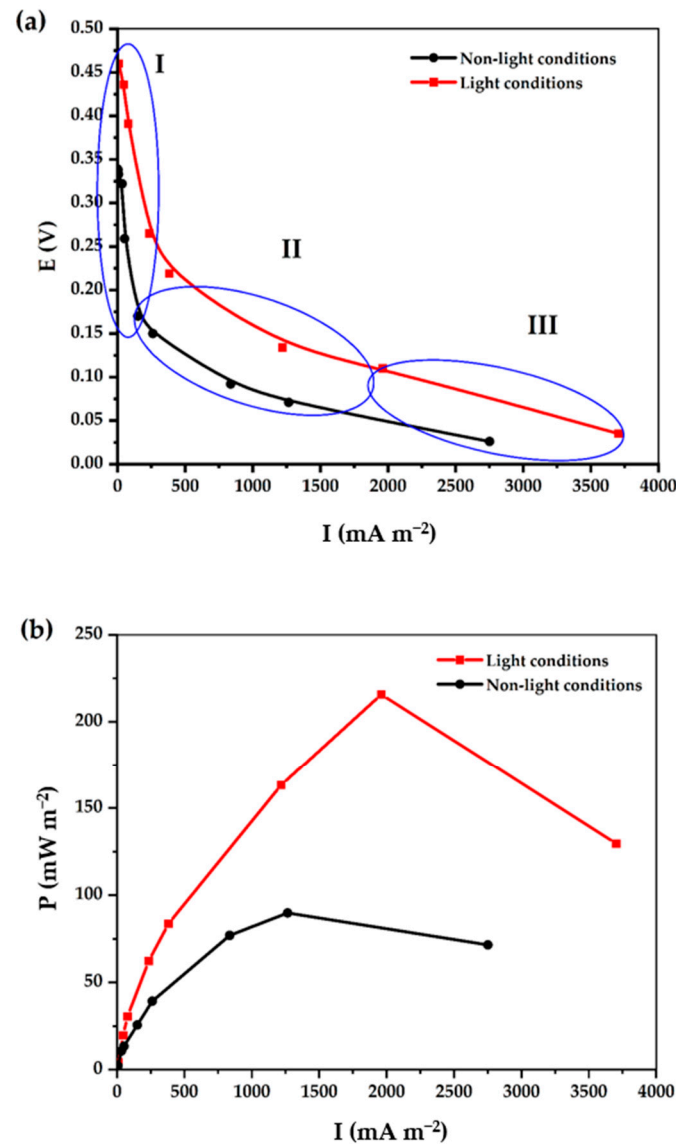


Figure 6. (a) Polarization curves and (b) power density for  $\text{Li}_{0.95}\text{Ta}_{0.76}\text{Nb}_{0.19}\text{Mg}_{0.15}\text{O}_3$ -based MFCs.

Table 1. Performance of MFCs equipped with the  $\text{Li}_{0.95}\text{Ta}_{0.76}\text{Nb}_{0.19}\text{Mg}_{0.15}\text{O}_3$  cathode in the presence and absence of a light source.

Light Source	CODr after 168 h (%)	Power Density, $P_{\text{max}}$ ( $\text{mW m}^{-2}$ )	OCV (v)	$R_{\text{int}}$ ( $\Omega$ )
Without	83.0	109	340	311
With	95.74	228	470	411

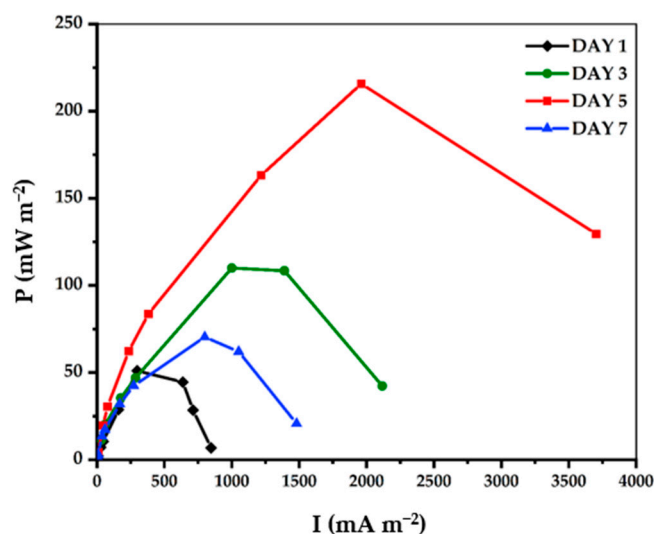


Figure 7. Power density variation of  $\text{Li}_{0.95}\text{Ta}_{0.76}\text{Nb}_{0.19}\text{Mg}_{0.15}\text{O}_3$  versus time under light conditions.

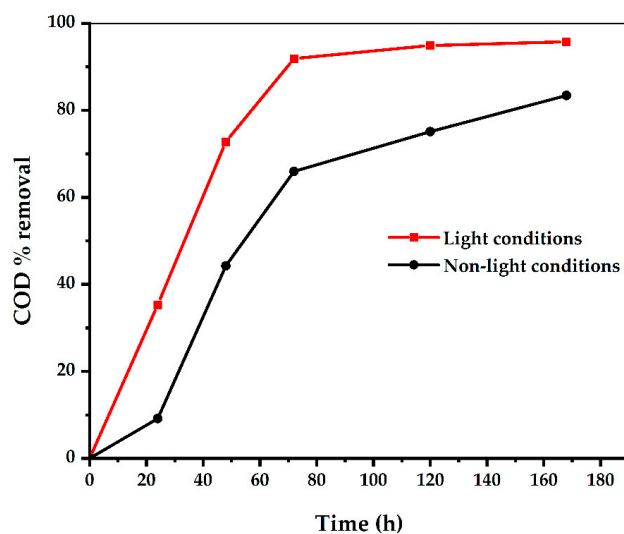
Referring to our previous work, the effect of non-stoichiometry on the photocatalytic activity of solid solutions based on  $\text{LiMO}_3$  iso-type materials ( $M = \text{Nb}, \text{Ta}$ ) modified with  $\text{Cu}^{2+}$  and  $\text{W}^{6+}$  was discussed [22,25,28,30,37]. Besides, Benzaouak et al. [37] tested non-stoichiometric  $\text{LiTa}_{1-x}\text{W}_x\text{O}_3$  ( $x \leq 0.25$ ) (LTW) iso-types of  $\text{LiTaO}_3$  materials in the same device, obtaining a maximum power output of  $107 \text{ mW m}^{-2}$  (Table 2), slightly lower than that of the LTNMg-based cathodes found in this work. Louki et al. [25,30] tested Cu-modified  $\text{LiTa}_{1-x}\text{Nb}_x\text{O}_3$  (LTNCu) solid-solution compositions, and they reported that the maximum power density generated in this case achieved  $200 \text{ mW m}^{-2}$ . It can be postulated that the difference in valency of the inserted ions leads to an excess of charges in materials containing  $2^+$  valence ions, in particular  $\text{Mg}^{2+}$ , which is favorable for a better charge transfer in the crystal lattice, creating an apparent polarization at the interface. Therefore, an improved charge carrier separation is expected, contributing to an increased photocatalytic performance [24,38].

Table 2. Comparison of recent results of photocatalysts tested in MFCs.

	$\lambda_{\text{max}}$ at Maximum Absorption (nm)	$E_g$ (eV)	CODr (mg L <sup>-1</sup> )	P (mW m <sup>-2</sup> )	OCV (mV)	$R_{\text{int}}$ ( $\Omega$ )	Specific Surface Area, m <sup>2</sup> g <sup>-1</sup>	References
LTNMg	330	4.03	95.7	228	460	228	4.06	This work
LTNCu	311	3.46	93	200	383	202	-	[30]
LTW	270	3.85	79	107	316	877	5.57	[37]

#### 2.4. Wastewater Treatment by Air-Cathode MFCs

The efficiency of LTNMg as a cathode in a MFC device was evaluated in terms of COD abatement and the lowering of heavy metals' content. Figure 8 displays the evolution of COD removal versus time in the MFC system using the LTNMg-based cathode in the presence and absence of the light source. After 24 h of operation, a significant COD reduction was achieved, attaining approximately 35% under irradiation, while under non-irradiative conditions, the MFC system reached only less than 10% of COD removal (Figure 8). After 72 h of operation time, the abatement extent was equal to 92% and 66% in the presence and absence of the light source, respectively. Thereafter, the COD removal slowly increased up to a final value of ~96% under light irradiation for 168 h, while without any light, a final value of ~83% was obtained. Overall, recorded data demonstrate a good wastewater treatment efficiency, especially under light conditions, which correlates well with the maximum power density results [39].



**Figure 8.** COD removal over time in MFC with the  $\text{Li}_{0.95}\text{Ta}_{0.76}\text{Nb}_{0.19}\text{Mg}_{0.15}\text{O}_3$  cathode in the presence and absence of a light source.

As further analysis, the removal efficiencies of heavy metals detected in the wastewaters used, including  $^{63}\text{Cu}$ ,  $^{111}\text{Cd}$ ,  $^{56}\text{Fe}$ , and  $^{52}\text{Cr}$ , were determined, and the initial concentration of each metal is reported in Table 3. As a general trend, higher metal removal efficiencies were attained at irradiation conditions, in which a higher power density was also achieved with respect to those values under no light. Specifically, the removal percentages were around 96% for  $^{63}\text{Cu}$ , 89% for  $^{56}\text{Fe}$ , 55% for  $^{52}\text{Cr}$ , and 17% for  $^{111}\text{Cd}$ . Generally, it is reported that bioactivity, biosorption, and bioaccumulation are important processes in heavy metals' removal in the presence of microbes [40,41]. The determination of the specific mechanisms controlling the heavy metal removal process is not the focus of this research, and there are several recently published articles referring to the removal of heavy metals in MFC systems. In fact, the presence of inorganic anions in the effluent may promote the removal of heavy metals by precipitation. Based on the slight pH variations observed in the anode chamber (pH 7.17–7.24), the precipitation of metals in the form of hydroxides appears to have no significant effect on the removal process in the analyzed system. In addition, another important process that may occur is the adsorption of heavy metals on the separator. The latter is composed of a polymeric containment membrane that has shown its ability to adsorb heavy metals such as Cd(II), Cu(II), and Fe(III) [42–44].

**Table 3.** Removal efficiencies of heavy metals from wastewater during LTNMg-based MFC operation for 168 h in the presence and absence of a light source.

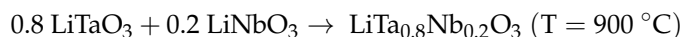
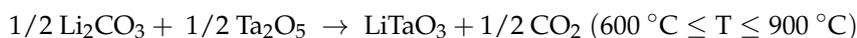
Metal Species	Initial Concentrations in Wastewater (ppb)	Removal Efficiencies of Heavy Metals (%)	
		Light Conditions	Non-Light Conditions
$^{63}\text{Cu}$	9.250	96.92	48.00
$^{111}\text{Cd}$	0.390	17.29	11.10
$^{56}\text{Fe}$	35.153	89.12	31.23
$^{52}\text{Cr}$	0.530	55.54	9.37

### 3. Materials and Methods

#### 3.1. Catalyst Preparation and Crystalline Structure Characterization

The chemicals used for the syntheses of photocatalysts included:  $\text{Li}_2\text{CO}_3$  (99%),  $\text{Ta}_2\text{O}_5$  (99%),  $\text{Nb}_2\text{O}_5$  (99.5%), and  $\text{MgO}$  (99.9%), and the chemicals were weighted and mixed stoichiometrically and then subjected to heat treatments in a muffle furnace to prepare

the final products via the ceramic route. The synthesis of the photocatalytic material  $\text{Li}_{0.95}\text{Ta}_{0.76}\text{Nb}_{0.19}\text{Mg}_{0.15}\text{O}_3$  was carried out according to the reactions specified below:



The phases were prepared by slow cooling from 1100 °C to ambient temperature. The final color was white for LTNMg. The CO<sub>2</sub> weight loss occurred between 600 and 700 °C, and above this temperature the weight loss was 0.62%.

The purity of the prepared phases and their structures was characterized using X-ray diffraction (BRUKER D8 ADVANCE, using Cu-K $\alpha$  radiation  $\lambda = 1504 \text{ \AA}$ ).

The Curie–Weiss temperature has been determined using a thermogravimetry analysis coupled to differential scanning calorimetry (DSC) (TGA/DSC, METTLER TOLEDO, Barcelona, Spain). Microstructure analysis of the synthesized phase was determined by transmission electron microscopy (TEM, Tecnai G<sup>2</sup> Series, FEI Company, Hillsboro, OR, USA).

### 3.2. UV-Visible Absorption Spectroscopy

The absorption and transmittance data of the studied sample were recorded with a Perkin-Elmer Instrument lambda 900 UV/Vis/NIR spectrophotometer in the solid state.

The estimation of the bandgap of the studied material was determined from the absorbance spectrum using Tauc's equation:

$$(\alpha h\nu) = A(h\nu - E_g)^n$$

where  $E_g$  is the bandgap energy of the material,  $\nu$  is the frequency of the incident radiation,  $h$  is Planck's constant,  $A$  is a constant related to the material, the coefficient  $n$  refers to the nature of the transition ( $n = 1/2$  for direct gap), and  $\alpha$  is the absorption coefficient in  $\text{cm}^{-1}$ , calculated by using the following equation:

$$I = I_0 e^{-\alpha t}$$

where  $I_0$  and  $I$  are the incident and transmitted intensities, respectively.

### Air-Cathode MFC Setup and Operation

The prepared  $\text{Li}_{0.95}\text{Ta}_{0.76}\text{Nb}_{0.19}\text{Mg}_{0.15}\text{O}_3$  (LTNMg) were assessed in single-chamber MFCs (Figure 9) consisting of glass bottle reactors of 250 mL anode capacity and equipped with an external jacket, to keep the operating temperature constant at 25 °C with a thermostatic bath. The cathode consisted of a mixture of the respective synthesized phases as catalysts and a solution of polytetrafluoroethylene (PTFE) as a binder (solid, Sigma-Aldrich, Burlington, MA, USA), mechanically pressed onto a piece of carbon cloth ( $1 \text{ cm}^2$ ). The total loading was  $60 \text{ mg cm}^{-2}$  in a 1:9 mass ratio of PTFE:oxide. The anode comprises 100 g of graphite granules of 2–6 mm in diameter and a graphite rod of 3.18 mm in diameter, which is externally connected to the cathode with a resistance load of 1 k $\Omega$ . MFC tests were run in batch mode. The anode chamber was loaded with 125 mL of industrial wastewater (sampled from mineral oil refinery) containing a mixture of microorganisms, with *Escherichia coli* in the majority. All reactors were setup with a proton exchange membrane (Nafion 117) of 4 cm in diameter placed between the cathode and the anode chamber, as explained in [45]. The experiment was conducted at 27 °C for 168 h. The surface of  $1 \text{ cm}^2$  that contained active phase was irradiated with a UV-visible lamp, placed at a distance of 20 cm from the cathode. The specific power measured by a solarimeter was close to  $480 \text{ W m}^{-2}$ .



**Figure 9.** Schematic illustration of the MFC setup.

### 3.3. Electrochemical Characterization and Analysis

Polarization measurement was conducted to determine the generation of MFC at different external resistances (11 M $\Omega$ –1  $\Omega$ ) using an external resistor. The polarization curves were obtained from the corresponding voltage data. The open-circuit voltages (OCVs) of air-cathode MFCs were measured using a voltage meter. The current density (I) was given by:  $I = \frac{V_{\text{voltage}}}{R_{\text{external}}}$ , and the power density (P) was calculated by the following relationship:  $P = V \times I$ , where I and P are normalized to the surface of the catalyst.

### 3.4. COD Removal Efficiency and Heavy Metals' Analysis

The chemical oxygen demand (COD) was performed as mentioned in the APHA protocol [46,47], employing a spectrophotometer, Spectroquant Nova 30 (Merck, Germany), and calculated with the following equation:

$$COD_{\text{removal}} = \frac{[C]_{\text{initial}} - [C]_{\text{final}}}{[C]_{\text{initial}}} \times 100\% \quad (2)$$

where  $[C]_{\text{initial}}$  = initial COD (mg/L) of the effluent in the anode chamber and  $[C]_{\text{final}}$  = COD of the effluent (mg/L) in the anode chamber at the end of the experiment.

Analysis of heavy metals ( $^{56}\text{Fe}$ ,  $^{52}\text{Cr}$ ,  $^{111}\text{Cd}$ , and  $^{63}\text{Cu}$ ) in wastewater was performed by ICP-MS Agilent 7500ce (Agilent Technologies, Santa Clara, CA, USA), equipped with an auto-sampler, ASX-510 (Cetac Technologies Inc., Omaha, NE, USA). The pH was determined using a digital pH meter (Crison Instruments, Barcelona, Spain) calibrated before each measurement. The wastewater-treated samples had a COD of about  $471 \pm 3$  mg/L and a pH of about  $7.24 \pm 0.2$ .

## 4. Conclusions

Performances of Mg-modified  $\text{LiNb}_{1-x}\text{Ta}_x\text{O}_3$  ( $x = 0.8$ ) as a cathode component in a single-chamber microbial fuel cell, using wastewater feedstock, were evaluated under sunlight irradiation and without a light source. The MFC efficiency was investigated in terms of electricity production and wastewater purification. The results obtained with the  $\text{Li}_{0.95}\text{Ta}_{0.76}\text{Nb}_{0.19}\text{Mg}_{0.15}\text{O}_3$  (LTNMg) ferroelectric cathode ceramic in the MFC device process showed a high COD removal of ~96% after a working time of 168 h, allowing the biofuel cells to produce a maximum power density of  $228 \text{ mW m}^{-2}$ . LTNMg performed much better under irradiation, reaching a maximum voltage of 470 mV in an open circuit. The structural and optoelectronic properties of the LTNMg ceramic promoted the cathodic efficiency during the MFC operation. The high performance of the MFC device was

attributed to the photocatalytic effect of  $\text{Li}_{0.95}\text{Ta}_{0.76}\text{Nb}_{0.19}\text{Mg}_{0.15}\text{O}_3$ , which improved the process of the cathodic electron transfer inside the MFC device.

The wastewater purification effectiveness was checked in terms of heavy metals' removal, particularly for  $^{63}\text{Cu}$ ,  $^{111}\text{Cd}$ ,  $^{56}\text{Fe}$ , and  $^{52}\text{Cr}$ . The highest removal percentage was around 96% for  $^{63}\text{Cu}$ , with the lowest efficiency being 17% for  $^{111}\text{Cd}$ .

In conclusion,  $\text{Li}_{0.95}\text{Ta}_{0.76}\text{Nb}_{0.19}\text{Mg}_{0.15}\text{O}_3$  showed remarkable electro- and photocatalytic performance in the MFC bifunctional process, producing a high wastewater purification and efficient electric production under visible light. This ceramic appears to be a promising alternative cathode component in a new generation of MFC devices.

**Author Contributions:** All the authors have contributed to the achievement of this work. N.T. and A.B. provided preparation and characterization of the catalyst, performed experiments, and wrote parts of the paper; A.E.H. helped with characterization techniques; M.E.M. is the Head of the ENSAM Research Team and oversaw investigation and validation; E.M.L. helped to find resources; M.K. designed the nature of catalyst; J.T. finalized the writing of the manuscript. L.F.L. contributed to funding the research and completed the writing of the manuscript in its final form. All authors have read and agreed to the published version of the manuscript.

**Funding:** This work was financially supported by the Moroccan Ministry of Higher Education, Scientific Research, and Innovation, and the OCP Foundation through the APRD research program.

**Acknowledgments:** We would like to thank the Moroccan Ministry of Higher Education, Scientific Research, and Innovation, and the OCP Foundation, who funded this work through the APRD research program. Part of this research was carried out by L.F.L. in the field of COST ACTION CA 18224 GREENERING "Green Chemical Engineering Network towards upscaling Sustainable Processes", and COST Action CA20127 "Waste biorefinery technologies for accelerating sustainable energy processes", supported by COST (European Cooperation in Science and Technology).

**Conflicts of Interest:** The authors declare no conflict of interest.

## References

1. Logan, B.E.; Hamelers, B.; Rozendal, R.; Schröder, U.; Keller, J.; Freguia, S.; Aelterman, P.; Verstraete, W.; Rabaey, K. Microbial Fuel Cells: Methodology and Technology. *Environ. Sci. Technol.* **2006**, *40*, 5181–5192. [[CrossRef](#)]
2. Yaqoob, A.A.; Khatoun, A.; Mohd Setapar, S.H.; Umar, K.; Parveen, T.; Mohamad Ibrahim, M.N.; Ahmad, A.; Rafatullah, M. Outlook on the Role of Microbial Fuel Cells in Remediation of Environmental Pollutants with Electricity Generation. *Catalysts* **2020**, *10*, 819. [[CrossRef](#)]
3. Yang, S.; Jia, B.; Liu, H. Effects of the Pt loading side and cathode-biofilm on the performance of a membrane-less and single-chamber microbial fuel cell. *Bioresour. Technol.* **2009**, *100*, 1197–1202. [[CrossRef](#)] [[PubMed](#)]
4. Chen, J.; Yang, J.; Wang, R.; Yang, Y.; Liu, Y. Design and research progress of nano materials in cathode catalysts of microbial fuel cells: A review. *Int. J. Hydrogen Energy* **2022**, *47*, 18098–18108. [[CrossRef](#)]
5. Qiu, S.; Guo, Z.; Naz, F.; Yang, Z.; Yu, C. An overview in the development of cathode materials for the improvement in power generation of microbial fuel cells. *Bioelectrochemistry* **2021**, *141*, 107834. [[CrossRef](#)]
6. Wang, H.; Wei, L.; Shen, J. Iron-gelatin aerogel derivative as high-performance oxygen reduction reaction electrocatalysts in microbial fuel cells. *Int. J. Hydrogen Energy* **2022**, *47*, 17982–17991. [[CrossRef](#)]
7. Lu, A.; Li, Y.; Jin, S.; Ding, H.; Zeng, C.; Wang, X.; Wang, C. Microbial Fuel Cell Equipped with a Photocatalytic Rutile-Coated Cathode. *Energy Fuels* **2010**, *24*, 1184–1190. [[CrossRef](#)]
8. Qian, F.; Wang, G.; Li, Y. Solar-Driven Microbial Photoelectrochemical Cells with a Nanowire Photocathode. *Nano Lett.* **2010**, *10*, 4686–4691. [[CrossRef](#)]
9. Gao, Y.; Ding, X.; Liu, J.; Wang, L.; Lu, Z.; Li, L.; Sun, L. Visible Light Driven Water Splitting in a Molecular Device with Unprecedentedly High Photocurrent Density. *J. Am. Chem. Soc.* **2013**, *135*, 4219–4222. [[CrossRef](#)]
10. Ma, J.; Chen, D.; Zhang, W.; An, Z.; Zeng, K.; Yuan, M.; Shen, J. Enhanced performance and degradation of wastewater in microbial fuel cells using titanium dioxide nanowire photocathodes. *RSC Adv.* **2021**, *11*, 2242–2252. [[CrossRef](#)]
11. Khan, M.E.; Khan, M.M.; Min, B.-K.; Cho, M.H. Microbial fuel cell assisted band gap narrowed  $\text{TiO}_2$  for visible light-induced photocatalytic activities and power generation. *Sci. Rep.* **2018**, *8*, 1723. [[CrossRef](#)] [[PubMed](#)]
12. Shaham-Waldmann, N.; Paz, Y. Away from  $\text{TiO}_2$ : A critical minireview on the developing of new photocatalysts for degradation of contaminants in water. *Mater. Sci. Semicond. Process.* **2016**, *42*, 72–80. [[CrossRef](#)]
13. Ge, J.; Zhang, Y.; Heo, Y.-J.; Park, S.-J. Advanced design and synthesis of composite photocatalysts for the remediation of wastewater: A review. *Catalysts* **2019**, *9*, 122. [[CrossRef](#)]

14. Ray, S.K.; Cho, J.; Hur, J. A critical review on strategies for improving efficiency of BaTiO<sub>3</sub>-based photocatalysts for wastewater treatment. *J. Environ. Manag.* **2021**, *290*, 112679. [[CrossRef](#)]
15. Cui, Y.; Briscoe, J.; Dunn, S. Effect of Ferroelectricity on Solar-Light-Driven Photocatalytic Activity of BaTiO<sub>3</sub>—Influence on the Carrier Separation and Stern Layer Formation. *Chem. Mater.* **2013**, *25*, 4215–4223. [[CrossRef](#)]
16. Ge, J.; Zhang, Y.; Park, S.-J. Recent Advances in Carbonaceous Photocatalysts with Enhanced Photocatalytic Performances: A Mini Review. *Materials* **2019**, *12*, 1916. [[CrossRef](#)]
17. Singh, G.; Sharma, M.; Bowen, C.; Vaish, R. 12—Ferroelectric ceramics and glass ceramics for photocatalysis. In *Ceramic Science and Engineering*; Misra, K.P., Misra, R.D.K., Eds.; Elsevier: Amsterdam, The Netherlands, 2022; pp. 297–322.
18. Djellabi, R.; Ordonez, M.F.; Conte, F.; Falletta, E.; Bianchi, C.L.; Rossetti, I. A review of advances in multifunctional XTiO<sub>3</sub> perovskite-type oxides as piezo-photocatalysts for environmental remediation and energy production. *J. Hazard. Mater.* **2022**, *421*, 126792. [[CrossRef](#)]
19. Miller, R.C.; Savage, A. Temperature dependence of the optical properties of ferroelectric LiNbO<sub>3</sub> and LiTaO<sub>3</sub>. *Appl. Phys. Lett.* **1966**, *9*, 169–171. [[CrossRef](#)]
20. Abrahams, S.C.; Kurtz, S.K.; Jamieson, P.B. Atomic Displacement Relationship to Curie Temperature and Spontaneous Polarization in Displacive Ferroelectrics. *Phys. Rev.* **1968**, *172*, 551–553. [[CrossRef](#)]
21. Benzaouak, A.; Ellouzi, I.; Ouanji, F.; Touach, N.; Kacimi, M.; Ziyad, M.; El Mahi, M.; Lotfi, E.M. Photocatalytic degradation of Methylene Blue (MB) dye in aqueous solution by ferroelectric Li<sub>1-x</sub>Ta<sub>1-x</sub>W<sub>x</sub>O<sub>3</sub> materials. *Colloids Surf. A Physicochem. Eng. Asp.* **2018**, *553*, 586–592. [[CrossRef](#)]
22. Touach, N.; Ortiz-Martínez, V.M.; Salar-García, M.J.; Benzaouak, A.; Hernández-Fernández, F.P.; de Ríos, A.; El Mahi, M.; Lotfi, E.M. On the use of ferroelectric material LiNbO<sub>3</sub> as novel photocatalyst in wastewater-fed microbial fuel cells. *Particuology* **2017**, *34*, 147–155. [[CrossRef](#)]
23. Khan, M.A.; Nadeem, M.A.; Idriss, H. Ferroelectric polarization effect on surface chemistry and photo-catalytic activity: A review. *Surf. Sci. Rep.* **2016**, *71*, 1–31. [[CrossRef](#)]
24. Stock, M.; Dunn, S. Influence of the Ferroelectric Nature of Lithium Niobate to Drive Photocatalytic Dye Decolorization under Artificial Solar Light. *J. Phys. Chem. C* **2012**, *116*, 20854–20859. [[CrossRef](#)]
25. Louki, S.; Touach, N.E.; Benzaouak, A.; Salar-García, M.J.; Ortiz-Martínez, V.M.; Hernández-Fernández, F.J.; de los Ríos, A.P.; El Mahi, M.; Lotfi, E.M. Preparation of new ferroelectric Li<sub>0.95</sub>Ta<sub>0.57</sub>Nb<sub>0.38</sub>Cu<sub>0.15</sub>O<sub>3</sub> materials as photocatalysts in microbial fuel cells. *Can. J. Chem. Eng.* **2018**, *96*, 1656–1662. [[CrossRef](#)]
26. Reichenbach, P.; Kämpfe, T.; Thiessen, A.; Schröder, M.; Haußmann, A.; Woike, T.; Eng, L. Multiphoton-induced luminescence contrast between antiparallel ferroelectric domains in Mg-doped LiNbO<sub>3</sub>. *J. Appl. Phys.* **2014**, *115*, 213509. [[CrossRef](#)]
27. Reichenbach, P.; Kämpfe, T.; Thiessen, A.; Haußmann, A.; Woike, T.; Eng, L. Multiphoton photoluminescence contrast in switched Mg: LiNbO<sub>3</sub> and Mg: LiTaO<sub>3</sub> single crystals. *Appl. Phys. Lett.* **2014**, *105*, 122906. [[CrossRef](#)]
28. Benzaouak, A.; Touach, N.; Ortiz-Martínez, V.M.; Salar-García, M.J.; Hernández-Fernández, F.J.; Perez de los Rios, A.; Mahi, M.E.; Lotfi, E.M. Ferroelectric LiTaO<sub>3</sub> as novel photo-electrocatalyst in microbial fuel cells. *Environ. Prog. Sustain. Energy* **2017**, *36*, 1568–1574. [[CrossRef](#)]
29. Kamali, A.R.; Fray, D.J. Preparation of lithium niobate particles via reactive molten salt synthesis method. *Ceram. Int.* **2014**, *40*, 1835–1841. [[CrossRef](#)]
30. Louki, S.; Touach, N.; Benzaouak, A.; Ortiz-Martínez, V.; Salar-García, M.; Hernández-Fernández, F.; de los Ríos, A.; El Mahi, M.; Lotfi, E. Characterization of New Nonstoichiometric Ferroelectric (Li<sub>0.95</sub>Cu<sub>0.15</sub>) Ta<sub>0.76</sub>Nb<sub>0.19</sub>O<sub>3</sub> and Comparative Study With (Li<sub>0.95</sub>Cu<sub>0.15</sub>) Ta<sub>0.57</sub>Nb<sub>0.38</sub>O<sub>3</sub> as Photocatalysts in Microbial Fuel Cells. *J. Electrochem. Energy Convers. Storage* **2019**, *16*, 021009. [[CrossRef](#)]
31. Choudhury, P.; Bhunia, B.; Mahata, N.; Bandyopadhyay, T.K. Optimization for the improvement of power in equal volume of single chamber microbial fuel cell using dairy wastewater. *J. Indian Chem. Soc.* **2022**, *99*, 100489. [[CrossRef](#)]
32. ElMekawy, A.; Hegab, H.M.; Dominguez-Benetton, X.; Pant, D. Internal resistance of microfluidic microbial fuel cell: Challenges and potential opportunities. *Bioresour. Technol.* **2013**, *142*, 672–682. [[CrossRef](#)] [[PubMed](#)]
33. Radeef, A.Y.; Ismail, Z.Z. Polarization model of microbial fuel cell for treatment of actual potato chips processing wastewater associated with power generation. *J. Electroanal. Chem.* **2019**, *836*, 176–181. [[CrossRef](#)]
34. Fan, Y.; Sharbrough, E.; Liu, H. Quantification of the Internal Resistance Distribution of Microbial Fuel Cells. *Environ. Sci. Technol.* **2008**, *42*, 8101–8107. [[CrossRef](#)] [[PubMed](#)]
35. Lun, M.; Zhou, X.; Hu, S.; Hong, Y.; Wang, B.; Yao, A.; Li, W.; Chu, B.; He, Q.; Cheng, J.; et al. Ferroelectric K<sub>0.5</sub>Na<sub>0.5</sub>NbO<sub>3</sub> catalysts for dye wastewater degradation. *Ceram. Int.* **2021**, *47*, 28797–28805. [[CrossRef](#)]
36. Xu, Z.; Chen, S.; Guo, S.; Wan, D.; Xu, H.; Yan, W.; Jin, X.; Feng, J. New insights in light-assisted microbial fuel cells for wastewater treatment and power generation: A win-win cooperation. *J. Power Sources* **2021**, *501*, 230000. [[CrossRef](#)]
37. Benzaouak, A.; Touach, N.-E.; Ortiz-Martínez, V.M.; Salar-García, M.J.; Hernández-Fernández, F.; de los Ríos, A.P.; Mahi, M.E.; Lotfi, E.M. Ferroelectric solid solution Li<sub>1-x</sub>Ta<sub>1-x</sub>W<sub>x</sub>O<sub>3</sub> as potential photocatalysts in microbial fuel cells: Effect of the W content. *Chin. J. Chem. Eng.* **2018**, *26*, 1985–1991. [[CrossRef](#)]
38. Wang, X.; Yan, W.; Zhang, Y.; Zhang, L.; Shi, L.; Huang, Y.; Wu, M.; Wang, X.; Chen, H. Threshold effect in the Mg-doping dependence of the photocatalytic ability of LiNbO<sub>3</sub> nanoparticles. *J. Am. Ceram. Soc.* **2017**, *100*, 739–745. [[CrossRef](#)]

39. Chen, P.; Zhang, T.; Chen, Y.; Ma, H.; Wang, Y.; Liu, W.; Wang, Y.; Zhou, G.; Qing, R.; Zhao, Y.; et al. Integrated chamber-free microbial fuel cell for wastewater purification and bioenergy generation. *Chem. Eng. J.* **2022**, *442*, 136091. [[CrossRef](#)]
40. Noori, M.T.; Thatikayala, D.; Pant, D.; Min, B. A critical review on microbe-electrode interactions towards heavy metal ion detection using microbial fuel cell technology. *Bioresour. Technol.* **2022**, *347*, 126589. [[CrossRef](#)]
41. Zhang, J.; Jiao, W.; Huang, S.; Wang, H.; Cao, X.; Li, X.; Sakamaki, T. Application of microbial fuel cell technology to the remediation of compound heavy metal contamination in soil. *J. Environ. Manag.* **2022**, *320*, 115670. [[CrossRef](#)]
42. Yaqoob, A.A.; Ibrahim, M.N.M.; Guerrero-Barajas, C. Modern trend of anodes in microbial fuel cells (MFCs): An overview. *Environ. Technol. Innov.* **2021**, *23*, 101579. [[CrossRef](#)]
43. Zhu, H.; Hu, X.; Zha, Z.; Cai, F.; Zhou, Y.; Zhou, S.; Yao, J.; Zhang, Z. Long-time enrofloxacin processing with microbial fuel cells and the influence of coexisting heavy metals (Cu and Zn). *J. Environ. Chem. Eng.* **2022**, *10*, 107965. [[CrossRef](#)]
44. Yaqoob, A.A.; Ibrahim, M.N.M.; Umar, K. Biomass-derived composite anode electrode: Synthesis, characterizations, and application in microbial fuel cells (MFCs). *J. Environ. Chem. Eng.* **2021**, *9*, 106111. [[CrossRef](#)]
45. Hernández-Fernández, F.J.; Pérez de los Ríos, A.; Mateo-Ramírez, F.; Godínez, C.; Lozano-Blanco, L.J.; Moreno, J.I.; Tomás-Alonso, F. New application of supported ionic liquids membranes as proton exchange membranes in microbial fuel cell for waste water treatment. *Chem. Eng. J.* **2015**, *279*, 115–119. [[CrossRef](#)]
46. Larrosa-Guerrero, A.; Scott, K.; Head, I.M.; Mateo, F.; Ginesta, A.; Godínez, C. Effect of temperature on the performance of microbial fuel cells. *Fuel* **2010**, *89*, 3985–3994. [[CrossRef](#)]
47. Rice, E.W.; Baird, R.B.; Eaton, A.D.; Clesceri, L.S. *Standard Methods for the Examination of Water and Wastewater*; American Public Health Association: Washington, DC, USA, 2012; Volume 10.